

CDPM: Convolutional Deformable Part Models for Person Re-identification

Kan Wang, Changxing Ding, Stephen J. Maybank, and Dacheng Tao

Abstract—Part-level representations are essential for robust person re-identification. Due to errors in pedestrian detection, there are usually severe mis-alignment problems for body parts, which degrade the quality of part representations. To handle this problem, we propose a novel model named Convolutional Deformable Part Models (CDPM). CDPM works by decoupling the complex part alignment procedure into two easier steps. First, a vertical alignment step detects each part in the vertical direction with the help of a multi-task learning model. Second, a horizontal refinement step based on self-attention suppresses the background information around each detected body part. Since the two steps are performed orthogonally and sequentially, the difficulty of part alignment is significantly reduced. In the testing stage, CDPM is able to accurately align flexible body parts without the need of any outside information. Extensive experimental results justify the effectiveness of CDPM for part alignment. Most impressively, CDPM achieves state-of-the-art performance on three large-scale datasets: Market-1501, DukeMTMC-ReID, and CUHK03.

Index Terms—Person re-identification, alignment-robust recognition, part-based model, multi-task learning.

I. INTRODUCTION

PERSON re-identification (ReID) refers to the recognition of one pedestrian's identity from images captured by different cameras. Given an image containing a target pedestrian (the query), a ReID system attempts to search images that include the same pedestrian from a large set of pedestrian images (the gallery). ReID has received substantial attention from both academia and industry because of its wide-ranging application potentials, e.g., video surveillance and cross-camera tracking [1]. However, due to the large number of uncontrolled sources of variation, such as dramatic changes of pose and viewpoint, complex variations in illumination, as well as poor image quality, ReID remains a very challenging task.

The key of a robust ReID system lies in the quality of pedestrian representations. Many approaches [2], [3] attempt to extract holistic-level feature from the whole image directly. However, they usually suffer from the overfitting problem [4]. Recently, part-level representations have been proved to

Kan Wang and Changxing Ding are with the School of Electronic and Information Engineering, South China University of Technology, 381 Wushan Road, Tianhe District, Guangzhou 510000, P.R. China. (e-mail: eekan.wang@mail.scut.edu.cn; chxding@scut.edu.cn).

Stephen J. Maybank is with the Department of Computer Science and Information Systems, Birkbeck College, London WC1E 7HX, U.K. (e-mail: sjmaybank@dcs.bbk.ac.uk).

Dacheng Tao is with UBTech Sydney Artificial Intelligence Institute and the School of Information Technologies in the Faculty of Engineering and Information Technologies, The University of Sydney, Darlingtown, NSW 2008, Australia. (e-mail: dacheng.tao@sydney.edu.au).

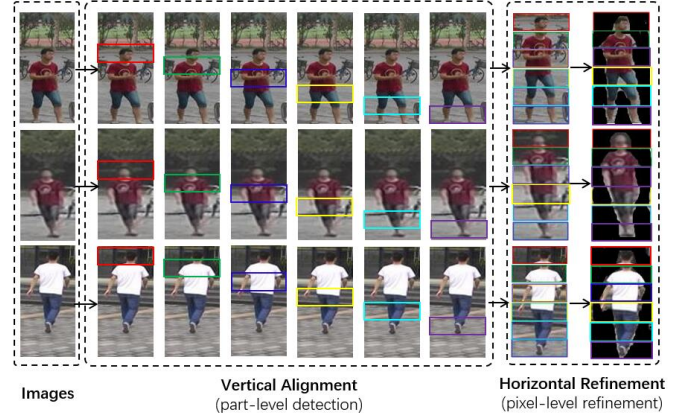


Fig. 1. The inference pipeline of CDPM. It decouples the part alignment problem into two easier steps, i.e., a vertical alignment step and a horizontal refinement step. Best viewed in color.

be highly discriminative and achieved state-of-the-art performance [5]–[9]. Due to errors in pedestrian detection [10], [11], the location of each body part varies in normalized images, as illustrated in Fig. 1. This phenomenon dramatically degrades the quality of part-level representations.

One intuitive strategy is to directly detect body parts using outside tools in both training and testing stages, e.g., keypoints produced by pose estimation algorithms [12], [13]. However, the predictions by outside tools may not be reliable enough since they are usually trained on databases whose images were captured under different conditions from ReID datasets. Another popular strategy is to detect body parts via self-attention models that are integrated seamlessly in the ReID architecture [6], [14]–[16]. However, the attention models are optimized by the ReID task only; therefore, they lack explicit guidance for part alignment.

In this paper, we propose a novel framework for part alignment. By providing the training stage with a minimal extra annotation (the upper and lower boundaries of a pedestrian) on the training set, we are able to factorize the complicated part alignment problem into two simpler and sequential steps, i.e., a vertical alignment step that detects body parts in the vertical direction and a horizontal refinement step that suppresses the background information around each detected part, as illustrated in Fig. 1.

Based on the above idea, we introduce a novel end-to-end model named Convolutional Deformable Part Models (CDPM), which can both detect flexible body parts and extract high-quality part-level representations. CDPM is built on one

popular convolutional neural network (CNN) as backbone and constructs three new modules, i.e., a feature learning module that extracts part-level features, a vertical alignment module that detects body parts in the vertical direction via multi-task learning, and a horizontal refinement module based on self-attention mechanism.

Different channels in CNN describe different visual patterns [4], [17], [18], i.e., different body parts in ReID. In other words, channel-wise responses provide hints of the location for each part. Therefore, CDPM succinctly integrates the above three modules together, based on the output of the same backbone model. In the inference stage, the vertical alignment module and the horizontal refinement module run sequentially for part alignment, followed by high-quality feature extraction from aligned parts.

The effectiveness of the proposed method is systematically evaluated on three popular ReID databases, i.e., Market-1501 [19], DukeMTMC-reID [20], and CUHK03 [21]. Experimental results show that CDPM achieves superior performance consistently and outperforms state-of-the-art approaches by a considerable margin.

Our contributions are summarized as threefold:

- We formulate the novel idea of decoupling the body-part alignment problem into two orthogonal and sequential steps, i.e., a vertical detection step and a horizontal refinement step. These two steps establish a novel framework for learning high-quality part-level representations. To the best of our knowledge, this is the first attempt that solves the mis-alignment problem by decomposition into orthogonal directions.
- Under the *divide-and-conquer* formulation, we propose a succinct CDPM architecture that integrates representation learning and part alignment by sharing the same backbone model. In particular, the vertical alignment module is realized by an elaborately designed multi-task learning structure.
- Extensive evaluation on three large-scale datasets demonstrate the superiority of CDPM. We also provide comprehensive ablation study to analyze the effectiveness of each component in CDPM.

The remainder of this paper is organized as follows. First, we review the related works in Section II. Then, we describe CDPM in detail in Section III. Extensive experimental results on three benchmarks are reported and analyzed in Section IV, leading to conclusions in Section V.

II. RELATED WORK

A. Person Re-identification

Prior to the prevalence of deep learning, approaches for ReID can be divided into two independent categories, i.e., methods for feature engineering [22], [23] and methods for metric learning [24]–[28]. In the past few years, deep learning-based approaches [4]–[9], [12], [13], [29]–[33] have dominated the ReID community. Many works target learning discriminative representations from the holistic image directly. One common strategy is to train deep models to learn ID-discriminative embedding (IDE) as an image classification

task [2]. Besides, the quality of image representations can be enhanced by metric learning-based loss functions, e.g., contrastive loss [34], triplet loss [35], and quadruplet loss [36]. There are also works that train deep models with combinations of different types of loss functions [37], [38].

The holistic image-based approaches usually suffer from the overfitting problem [4]. To relieve this problem, part-based approaches [4]–[8], [14] have been proposed to learn discriminative image representations and achieved state-of-the-art performance. However, due to errors in pedestrian detection, the location of each body part in different images varies. According to the strategy to handle the part mis-alignment problem, existing approaches can be grouped into three categories.

1) *Pre-defined Part Location-based Methods*: These approaches extract part-level features from patches [39] or horizontal stripes [5], [8], [40] of pre-defined locations. For example, Cheng *et al.* [40] uniformly divide a pedestrian image into 4 horizontal stripes from which part-level features are extracted. Wang *et al.* [5] also partition one image into horizontal stripes. It relieves the part mis-alignment problem by extracting multi-granularity part-level features. The above methods usually assume the mis-alignment problem is moderate; therefore they may have difficulty in handling severe mis-alignment cases.

2) *Outside Information-based Methods*: These methods align body parts by means of outside information, e.g., masks produced by human parsing tools [41]–[43] or keypoints detected by pose estimation algorithms [12], [13], [44]. Outside information is usually required in both training and testing stages [12], [13], [43]. The downside are first, there is extra computational cost, and second, the accuracy of part alignment depends on the outside tools, which are usually trained on databases whose images were captured under quite different conditions from ReID databases.

3) *Attention Model-based Methods*: These methods learn to predict bounding boxes or soft masks for body parts directly from feature maps produced by ReID networks, without any outside supervision [6], [14], [16], [17]. For example, Li *et al.* [6] designed a hard regional attention model that can predict bounding boxes for each body part. In comparison, Zhao *et al.* [16] proposed to predict a set of soft masks. Element-wise multiplication between one soft mask and each channel of feature maps produces part-level features. However, the lack of explicit supervision for part alignment may cause difficulty in the optimization of attention models.

The proposed CDPM approach improves the part alignment accuracy by introducing a minimal extra supervision in the training stage, by which the complicated part alignment problem can be decomposed into two separate and simpler steps. Therefore, compared with the attention-based methods, the optimization difficulty for part alignment is significantly reduced. Compared with the second category of methods, CDPM does not require any outside information in the testing stage; therefore it is easier to use in practice.

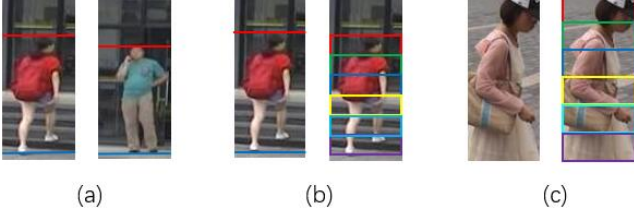


Fig. 2. (a) The provided extra annotation for the training set, i.e., the upper and lower boundaries of pedestrians. The red and blue lines indicate the upper and lower boundaries, respectively. This extra annotation is not required during the testing stage. (b) With the provided annotation, the location for each part can be inferred by uniform partition between the two boundaries. (c) When the annotation is not provided, we uniformly divide the whole image in the vertical direction. Best viewed in color.

B. Part-based Object Detection

Prior to the prevalence of deep learning, Deformable Part Model (DPM) was one of the most popular methods for object and pedestrian detection. In both DPM [45] and its deep versions [46]–[48], part detection is performed as an auxiliary task to promote the detection accuracy. In the past few years, region proposal-based methods [49], [50] have become more popular. Different from DPM, region proposal-based methods usually detect the whole object directly, without explicit part detection.

In comparison, the proposed method aims to detect flexible parts only, as the coarse location of the whole body is known. From this perspective, it is more similar to DPM than to region proposal-based methods. Since it is based on CNN, we name it Convolutional Deformable Part Models (CDPM).

III. CONVOLUTIONAL DEFORMABLE PART MODEL

A. Problem Formulation

As illustrated in Fig. 1, we decouple the complex part alignment problem into two separate and sequential steps, i.e., a vertical alignment step that locates each part in the vertical direction, and a horizontal refinement step that suppresses the background information around each part.

The first step is more challenging. First, the whole image is searched for each part. Second, there is usually no clear boundary between adjacent parts. We meet the above challenges by providing a minimal extra annotation as auxiliary supervision in the training stage. As shown in Fig. 2b, the upper and lower boundaries of pedestrians are labeled. The equal partition between the two boundaries produces the area of each part in the vertical direction. It is worth noting that annotation is not required in testing. Therefore, it can be regarded as a kind of privileged information [51]. In comparison, the second step is much easier; therefore it is not provided with any extra information.

Based on the above ideas, we propose the novel CDPM model for joint part feature learning and part alignment. As illustrated in Fig. 3, CDPM is built on the ResNet-50 backbone model [52]. Similar to [7], we remove the last spatial down-sampling operation in ResNet-50 to increase the size of the output feature maps. Based on these output feature maps, we construct three new modules, i.e., the feature learning module

for part-level feature extraction, the vertical alignment module based on multi-task learning, and the horizontal refinement module based on self-attention. The three modules work collaboratively to align body parts and further learn high-quality part-level representations.

B. Feature Learning Module

The feature learning module is based on one recent work named Part-based Convolutional Baseline (PCB) [7]. As illustrated in Fig. 3, the feature learning module incorporates K part-level feature learning branches, which learn part-specific features. The K branches share exactly the same structure, i.e., one Global Average Pooling (GAP) layer, one 1×1 convolutional layer, and one classification layer. In the training stage, the location for each part can be inferred from the provided annotations of the upper and lower pedestrian boundaries by uniform partition (Fig. 2b). If the upper or lower boundary is not provided, e.g., when they are invisible due to part missing (Fig. 2c), we uniformly divide the whole image in the vertical direction as in [7]. In the testing stage, the location of each part is determined via the proposed part alignment method.

Each of the K part-level features is optimized as a multi-class classification task using the softmax loss function. The loss function for the k -th part is formulated as:

$$L_p^k = -\frac{1}{N} \sum_{i=1}^N \log \frac{e^{\mathbf{w}_{y_i}^k T \mathbf{z}_i^k + b_{y_i}^k}}{\sum_{j=1}^C e^{\mathbf{w}_j^k T \mathbf{z}_i^k + b_j^k}}, \quad (1)$$

where \mathbf{w}_j^k is the weight vector for class j and b_j^k is the corresponding bias term. C denotes the number of classes in the training set. y_i and \mathbf{z}_i^k represent the label and the k -th part-level feature for the i -th image in a batch. Therefore, the overall loss function for the feature learning module is

$$L_f = \sum_{k=1}^K L_p^k. \quad (2)$$

C. Vertical Alignment Module

Different channels in feature maps produced by a ReID network describe different body parts [4], [18]. This indicates that the channel-wise responses provide hints of part location. We therefore design a detection module to locate body parts in the vertical direction, based on the output of the backbone model only. For simplicity, we divide the output of backbone model into R sliding windows with fixed height and width. Then, we select one sliding window for each part using the proposed vertical alignment module. In this paper, the size of output of the backbone model is $24 \times 8 \times 2048$, where the three dimensions denote height, width, and channel number, respectively. The size of each sliding window is set as $4 \times 8 \times 2048$; therefore R equals to 21 for each image.

Inspired by Faster R-CNN [50], we process the sliding windows by multi-task learning, i.e., coarse classification of all sliding windows, and refined regression of sliding windows to their respective ground-truth locations. The two tasks only share one GAP layer. It is worth noting that we only utilize images whose upper and lower boundaries are both annotated during training for this module.

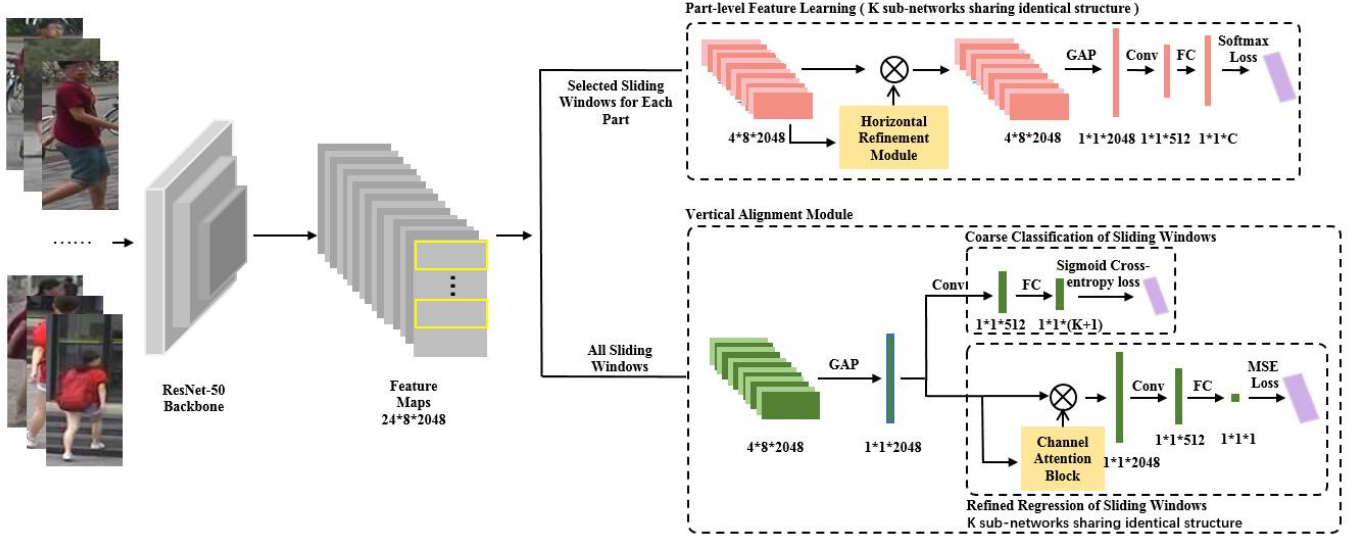


Fig. 3. Architecture of the proposed CDPM. Based on the ResNet-50 backbone model, CDPM constructs three new modules, i.e., the feature learning module including K part-level branches, the vertical alignment module, and the horizontal refinement module. In the inference stage, the vertical alignment module receives R sliding windows (denoted as yellow rectangles in the figure) for each image and selects one optimal sliding window for each part, respectively. The selected sliding window indicates the location of each part in the vertical direction. The horizontal refinement module further reduces the interference of background information in the selected sliding window. The above two modules work together to achieve the goal of part alignment, such that the part-level feature learning branches can learn robust features.

1) *Coarse Classification of Sliding Windows*: This task classifies all sliding windows to their corresponding parts or the background category. It incorporates one 1×1 convolutional layer and one fully-connected (FC) layer. Important parameters for the two layers are marked in Fig. 3. The output dimension of the FC layer is $K+1$, which denotes K parts and the background category. As each sliding window may overlap with two adjacent parts, their ground-truth labels are soft rather than one-hot. We therefore optimize the classification task using the sigmoid cross-entropy loss that can be formulated as $L_c =$

$$-\frac{1}{NR} \sum_{i=1}^N \sum_{r=1}^R \sum_{k=1}^{K+1} [y_i^{r(k)} \log \hat{y}_i^{r(k)} + (1 - y_i^{r(k)}) \log (1 - \hat{y}_i^{r(k)})], \quad (3)$$

where $y_i^{r(k)}$ is the ground-truth probability of the r -th sliding window belonging to the k -th part of the i -th image, and $\hat{y}_i^{r(k)}$ is the corresponding predicted probability value.

Ground-truth Label of Sliding Windows For a given sliding window $r(u_r, l_r)$ whose upper and lower boundaries are respectively u_r and l_r , we associate it with a ground-truth label vector $\mathbf{y}^r = (y^{r(1)}, y^{r(2)}, \dots, y^{r(K)}, y^{r(K+1)})$. The value of each element in \mathbf{y}^r depends on the size of overlap between r and the corresponding body part or the background category. Specifically, we first calculate the ground-truth upper and lower boundaries for the k -th part:

$$\begin{aligned} u_k &= U + (k-1) \times \frac{V-U}{K}, \\ l_k &= u_k + \frac{V-U}{K}, \end{aligned} \quad (4)$$

where U and V represent the annotated upper and lower boundaries of the pedestrian in the training image. We denote

the ground-truth area for the k -th part as $p_k(u_k, l_k)$. Then,

$$y^{r(k)} = \frac{S(p_k(u_k, l_k) \cap r(u_r, l_r))}{S(r(u_r, l_r))}, 1 \leq k \leq K, \quad (5)$$

and $y^{r(K+1)} = 1 - \sum_{k=1}^K y^{r(k)}$, where $S(*)$ denotes the size of the area $*$.

2) *Refined Regression of Sliding Windows*: We further promote the accuracy of the vertical alignment module via part-specific regression tasks. As illustrated in Fig. 3, the K regression tasks are constructed such that they all have the same structure. However, they do not share any parameters and each is optimized for the detection of one specific part.

Each regression task incorporates one channel attention block [53], one 1×1 convolutional layer, one FC layer, and one tanh layer. Important parameters for above layers are labeled in Fig. 3. The channel attention block is used to highlight the information for one specific part. Each channel attention block includes two successive 1×1 convolutional operations, whose important parameters are labeled in Fig. 4. The output of the sigmoid layer is channel attention. The input feature vector for the attention block is multiplied with channel attention in an element-wise manner. Finally, we get the weighted feature vector for each sliding window.

During training, the 2048-dim features of all sliding windows are fed into K regression branches, respectively. Correspondingly, we obtain K sets of predicted offsets after tanh normalization. Each regression task involves the optimization of the Mean Squared Error (MSE) loss:

$$L_r^k = \frac{1}{2\tilde{R}^k} \sum_{i=1}^N \sum_{j=1}^R (\Delta_j^{i(k)} - \hat{\Delta}_j^{i(k)})^2 \cdot \mathbf{1}\{|\Delta_j^{i(k)}| < 1\}, \quad (6)$$

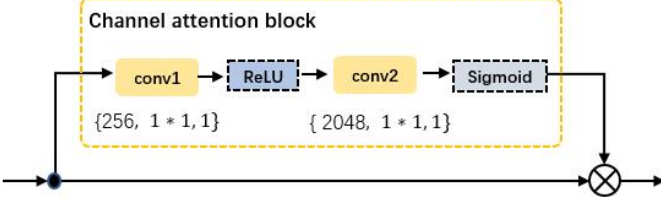


Fig. 4. Architecture of the adopted channel attention block. The three items in each bracket are: filter number, kernel size, and stride. Each convolutional layer is followed by a batch normalization layer, which is omitted for simplicity in the figure.

where $\Delta_j^{i(k)}$ denotes the ground-truth offset of the j -th sliding window for the k -th part in the i -th image and $\hat{\Delta}_j^{i(k)}$ is the corresponding predicted value. $\mathbf{1}\{|\Delta_j^{i(k)}| < 1\}$ equals to either 0 or 1, meaning that we only utilize sliding windows whose ground-truth offset value are within the range of $(-1, 1)$. \bar{R}^k denotes the number of sliding windows that satisfy $\mathbf{1}\{|\Delta_j^{i(k)}| < 1\}$ for all k -th parts in a mini-batch. $\Delta_j^{i(k)}$ can be easily obtained by first subtracting the sliding window's center coordinate in the vertical direction from that of the k -th part (Eq. 5), and then normalized by the height of the sliding window. Finally, the joint loss function for the vertical alignment module can be formulated as:

$$L_v = L_c + \sum_{k=1}^K L_r^k. \quad (7)$$

During testing, the 2048-dim features of all sliding windows are simultaneously fed into the classification task and K regression tasks. For each part, the classification scores and predicted offsets for the R sliding windows are obtained. We select the optimal sliding window for each part according to the following rules. First, if the classification scores of multiple sliding windows are above a pre-defined threshold T , then we select the one with the smallest offset (absolute value). Second, if there is only one or none sliding window whose classification score is above T , then we simply choose the one with the largest classification score.

D. Horizontal Refinement Module

The above module only detects body parts in the vertical direction. We further propose to suppress the background information in the K selected sliding windows via an extra horizontal refinement operation. As shown in Fig. 3, the horizontal refinement module is applied to each part-level feature learning branch, respectively. In this paper, we realize the module by the Spatial-Channel Attention (SCA) model proposed in [6].

For completeness, we briefly introduce the structure of SCA. As shown in Fig. 5, the spatial and channel attentions of SCA are realized by separate branches. The former branch consists of a global cross-channel average pooling layer, a convolutional layer, a resizing bilinear layer, and another convolutional layer. The latter branch consists of a GAP layer and two successive convolutional layers. Finally, the two types of attention information are fused by one convolutional layer

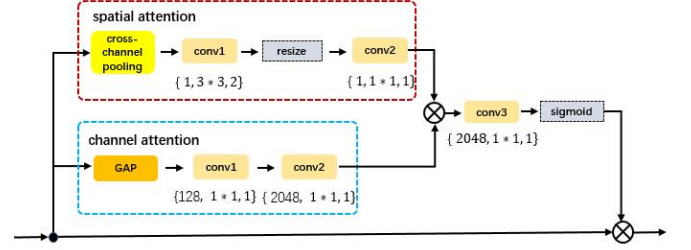


Fig. 5. Architecture of the Spatial-Channel Attention (SCA) model [6]. We utilize SCA to realize the horizontal refinement operation. The three items in each bracket are: filter number, kernel size, and stride. BN and ReLU layers after each convolutional layer are not shown for brevity. The value of all hyper-parameters of SCA remains the same as that in [6].

and normalized by one sigmoid layer. Important parameters of the SCA are marked in Fig. 5 and the rest of implementation details can be found in [6].

It is worth noting that SCA was originally employed to suppress the background information in the holistic pedestrian image [6], rather than around each body part. We argue that our *divide-and-conquer* strategy is more intuitive and effective, since it is dramatically easier to distinguish pixels of a single part from its surrounding background pixels. In comparison, applying SCA to the holistic image can be much more difficult, as both the structure of the whole body and the background information in the holistic image can be significantly more complicated.

E. Person Re-ID by CDPM

In the training stage, taking all three modules of CDPM into account, the overall objective function for CDPM can be written as

$$\begin{aligned} L &= L_f + L_v \\ &= \sum_{k=1}^K L_p^k + \lambda_1 * L_c + \lambda_2 * \sum_{k=1}^K L_r^k, \end{aligned} \quad (8)$$

where λ_1 and λ_2 are weights of loss functions. For simplicity, they are consistently set as 1 in this paper.

In the testing stage, each image passes through the backbone model and yields feature maps of size $24 \times 8 \times 2048$. For the part-level features, the $24 \times 8 \times 2048$ feature maps are divided into R sliding windows, whose size is fixed to $4 \times 8 \times 2048$. The vertical alignment module selects one optimal sliding window for each part. Then, the selected sliding window for the k -th part passes through the k -th horizontal refinement module and part-level feature learning branch to obtain the 512-dim part-level feature vector \mathbf{z}^k . The final representation of the image is obtained by concatenating the above K feature vectors:

$$\mathbf{f} = [\mathbf{z}^1, \mathbf{z}^2, \dots, \mathbf{z}^K]. \quad (9)$$

We consistently employ the cosine distance to calculate the similarity between two image representations.

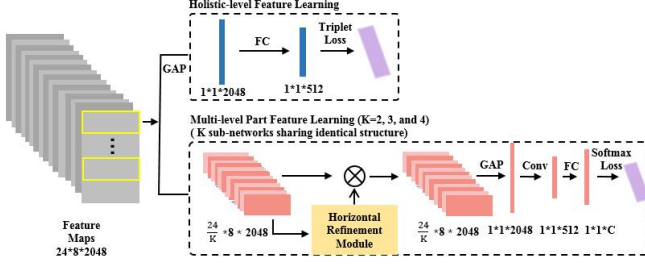


Fig. 6. New branches equipped by CDPM to extract multi-granularity features, which include one holistic-level feature learning branch, and 9 branches for multi-level part feature extraction.

F. Multi-granularity Feature

A few recent works [5], [8] adopt multi-granularity features (MGF) to boost the performance of ReID. Compared with single-level part features, MGF provides richer multi-scale information and therefore is more powerful. The CDPM framework is flexible and can naturally be extended to extract MGF, which include the holistic-level feature and multi-level part features.

1) *Holistic-level feature*: As shown in Fig. 6, the holistic-level feature learning branch is composed of one GAP layer and one FC layer with dimension 512. Similar to the part-level features, this branch is also attached to the output of the backbone model.

Following [5], the holistic-level feature is optimized by the triplet loss function, with the batch-hard triplet sampling policy [35]. To sample sufficient triplets in the training stage, we randomly sample A images in each of P random identities to compose a mini-batch. Therefore, the batchsize N equals to $P \times A$. For each anchor image, one triplet is constructed by selecting the furthest intra-class image in the feature space as positive and the closest inter-class image as negative. The triplet loss is formulated as $L_g =$

$$\frac{1}{2M} \sum_{i=1}^P \sum_{a=1}^A \left[\max_{p=1 \dots A} \|\mathbf{h}_i^a - \mathbf{h}_i^p\|_2^2 - \min_{\substack{n=1 \dots A \\ j \neq i}} \|\mathbf{h}_i^a - \mathbf{h}_j^n\|_2^2 + \alpha \right]_+, \quad (10)$$

where α denotes the margin for triplet constraint and M is the number of triplets $\{\mathbf{h}_i^a, \mathbf{h}_i^p, \mathbf{h}_j^n\}$ in a batch that violate the constraint [35]. \mathbf{h}_i^a , \mathbf{h}_i^p , and \mathbf{h}_j^n are L2-normalized holistic-level representations of the anchor, positive, and negative images in a triplet, respectively. $[*]_+ = \max(0, *)$ is the hinge loss.

2) *Multi-level part features*: We further add more part-level feature learning branches of other granularities. In detail, we set K as 2, 3, and 4, respectively. Therefore, there are 9 more part-level feature learning branches. As illustrated in Fig. 6, both the structure and loss function of the new branches are exactly the same as the original ones in CDPM.

It is worth noting that we only add more branches in the feature learning module. The vertical alignment module of CDPM remains unchanged. As explained in Fig. 7, in the testing stage, the location of each part of new granularities can

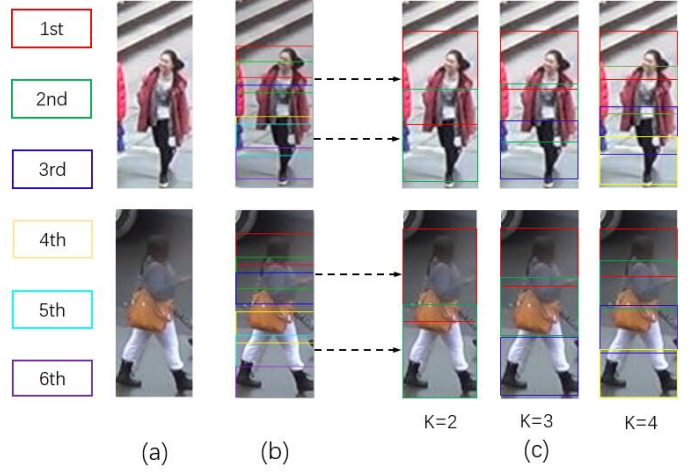


Fig. 7. The way to obtain the part location of new granularities in the testing stage. (a) The original images. (b) Predicted locations for parts of the original granularity by the vertical alignment module. (c) We infer the part location of new granularities from relevant parts in (b). For example, the center of the first part when K equals to 2 can be calculated by averaging the center locations of the first three parts in (b). We fix the size of parts of the same granularity. Best viewed in color.

be inferred from the prediction results of the original vertical alignment module in CDPM.

To compose MGF in the testing stage, we extract part-level features of all the above granularities as well as the holistic-level feature. All the above features are concatenated as the final representation for one pedestrian image.

IV. EXPERIMENTS

A. Datasets

To justify the effectiveness of CDPM, we conduct exhaustive experiments on three large-scale person ReID benchmarks, i.e., Market-1501 [19], DukeMTMC-ReID [20] and CUHK03 [21]. We follow the official evaluation protocol for each database. Besides, we report both the Rank-1 accuracy and mean Average Precision (mAP) for all three datasets.

Market-1501 contains 32,668 pedestrian images. The pedestrians were detected by a DPM-based algorithm. These images belong to 1,501 subjects and were captured by 6 cameras. The dataset is divided into two sets: a training set containing 12,936 images of 751 identities, and a testing set consisting of images of the remaining 750 identities. The testing set is further divided into a gallery set of 19,732 images and a query set of 3,368 images. Moreover, we report results under both single-query and multi-query settings.

DukeMTMC-ReID features dramatic variations of background and viewpoints. It contains 36,411 images of 1,404 identities. The images were captured by 8 cameras. The dataset is split into one training set containing 16,522 images of 702 identities, and one testing set composed of 17,661 gallery images and 2,228 query images of the remaining 702 identities.

CUHK03 includes 14,097 images of 1,467 identities. Images for each identity were captured by two cameras. The

dataset provides both hand-labeled and DPM-detected bounding boxes. We evaluate our method using both types of bounding boxes. Besides, we adopt the new train/test protocol proposed in [54]. The new protocol splits the dataset into a training set of 767 identities and a testing set of the remaining 700 identities.

B. Implementation Details

The naive combination of the backbone model and the feature learning module, i.e., the PCB model [7], is chosen as the baseline. Compared with CDPM, the baseline model lacks the part alignment ability. In this case, we uniformly divide feature maps produced by the backbone model in the vertical direction into K non-overlapped parts as the input for the part-level feature learning branches.

1) *Hyper-parameters of CDPM*: The number of body parts, i.e., K , is set as 6 following the baseline model [7]. Besides, the threshold value T for sliding window selection is empirically set as 0.60 for Market-1501 and 0.35 for the other two databases. Value of hyper-parameters of SCA remain the same as the original work [6]. Finally, when triplet loss is utilized for training, we set P as 6 and A as 8. The margin α for the triplet loss is set as 0.4.

2) *Training details*: Experiments are conducted using the PyTorch framework. All pedestrian images are resized to 384×128 pixels. Following existing works [21], [55], we adopt extensive data augmentation to reduce overfitting of deep models. Specifically, we augment the training data via offline translation [21], online horizontal flipping, and online random erasing [55]. After offline translation, each training set is enlarged by 5 times. Besides, the ratio of random erasing is set as 0.5.

We use the standard stochastic gradient descent with momentum [56] for model optimization and set the momentum value as 0.9. We set the batch size N as 48. Besides, we utilize a stage-wise strategy to train CDPM. In the first stage, we fine-tune the baseline model from the IDE model proposed in [2] for 50 epochs. The learning rate is set as 0.01 initially and multiplied by 0.1 for every 20 epochs. In the second stage, we fix the parameters of the baseline model, and only optimize the parameters of the newly introduced components in CDPM, i.e., the vertical alignment module and horizontal refinement modules. This stage is trained for 40 epochs, with learning rate set as 0.01 initially and multiplied by 0.1 for every 15 epochs. Finally, all CDPM model parameters are fine-tuned in the end-to-end fashion for 30 epochs, with a small initial learning rate of 0.001 and decreased to 0.0001 after 20 epochs.

C. Comparisons to State-of-the-Art Methods

The essential contribution of CDPM lies in detecting flexible body parts for ReID. For fair comparison with existing approaches, we categorize them into three groups, i.e., holistic feature-based methods, single-level part feature-based methods, and multi-granularity feature-based methods. We denote them as HF-based, SPF-based, and MGF, respectively.

1) *Evaluation on Market-1501*: Performance comparisons between CDPM and state-of-the-art methods on Market-1501 are tabulated in Table I. It is shown that CDPM significantly outperforms all existing methods for both Rank-1 and mAP results and achieves state-of-the-art performance. In particular, CDPM outperforms the most recent SPF-based method, i.e., PCB+RPP [7], by 1.5% and 4.6% on the single-query mode for Rank-1 accuracy and mAP, respectively. The above comparisons justify the effectiveness of CDPM. Besides, the performance of CDPM is further improved by extracting multi-granularity features. Finally, CDPM achieves state-of-the-art performance and beat all the other approaches. Specifically, CDPM achieves 95.9% and 87.3% for Rank-1 accuracy and mAP on the single-query mode, respectively.

TABLE I
PERFORMANCE COMPARISONS ON THE MARKET-1501 DATASET. BOTH RANK-1 ACCURACY (%) AND MAP (%) INDICES ARE COMPARED. CDPM* REFERS TO THE CDPM MODEL THAT EXTRACTS MULTI-GRANULARITY FEATURES FOR REID.

Query Type		Single Query		Multiple Query	
Methods		Rank-1	mAP	Rank-1	mAP
HF-based	SVDNet [57]	82.3	62.1	-	-
	PAN [11]	82.8	63.4	88.2	71.7
	MGCAM [41]	83.6	74.3	-	-
	Triplet Loss [35]	84.9	69.1	90.5	76.4
	DaRe [58]	86.4	69.3	-	-
	MLFN [59]	90.0	74.3	92.3	82.4
SPF-based	Spindle [12]	76.9	-	-	-
	MSCAN [14]	80.3	57.5	86.8	66.7
	PAR [16]	81.0	63.4	-	-
	PDC [13]	84.1	63.4	-	-
	AACN [44]	85.9	66.9	89.8	75.1
	AlignedReID [10]	91.8	79.3	-	-
	HA-CNN [6]	91.2	75.7	93.8	82.8
	PCB+RPP [7]	93.8	81.6	-	-
	CDPM	95.3	86.2	96.3	90.0
MGF	HPM [8]	94.2	82.7	-	-
	MGN [5]	95.7	86.9	96.9	90.7
	CDPM*	95.9	87.3	97.2	91.3

2) *Evaluation on DukeMTMC-ReID*: Compared with Market-1501, pedestrian images in DukeMTMC-ReID suffer from more variations in viewpoints and background. Performance comparisons are summarized in Table II. It is shown that CDPM achieves the best Rank-1 and mAP performance, outperforming all state-of-the-art methods by a large margin. In particular, CDPM outperforms the best existing SPF-based approach [60] by 4.0% and 8.3% on Rank-1 and mAP performance, respectively. The above results suggest that CDPM can locate body parts accurately even under dramatic variations in viewpoints and background.

3) *Evaluation on CUHK03*: We evaluate the performance of CDPM on CUHK03 using manually-labeled and auto-detected bounding boxes, respectively. Comparison results are tabulated in Table III. It is shown that CDPM achieves the best performance among SPF-based approaches. In particular, it outperforms the second-best approach [7] by 7.9% and 9.4% for Rank-1 and mAP accuracy using auto-detected bounding boxes, respectively. Besides, among MGF-based approaches, CDPM also achieves the best performance. The above comparisons firmly justify the effectiveness of CDPM.

TABLE II
PERFORMANCE COMPARISONS ON DUKEMTMC-REID. CDPM* REFERS TO THE CDPM MODEL THAT EXTRACTS MULTI-GRANULARITY FEATURES FOR REID.

Methods		Rank-1	mAP
HF-based	PAN [11]	71.6	51.5
	DaRe [58]	75.2	57.4
	SVDNet [57]	76.7	56.8
	MLFN [59]	81.0	62.8
SPF-based	AACN [44]	76.8	59.3
	HA-CNN [6]	80.5	63.8
	PCB+RPP [7]	83.3	69.2
	Part-aligned [60]	84.4	69.3
	CDPM	88.4	77.6
MGF	HPM [8]	86.6	74.3
	MGN [5]	88.7	78.4
	CDPM*	90.2	80.2

TABLE III
PERFORMANCE COMPARISONS ON THE CUHK03 DATASET, USING THE NEW PROTOCOL PROPOSED IN [54]. CDPM* REFERS TO THE CDPM MODEL THAT EXTRACTS MULTI-GRANULARITY FEATURES FOR REID.

Bounding Boxes Type		detected		labeled	
Methods		Rank-1	mAP	Rank-1	mAP
HF-based	PAN [58]	36.9	35.0	36.3	34.0
	DPFL [61]	43.0	40.5	40.7	37.0
	SVDNet [57]	41.5	37.3	40.9	37.8
	MGCAM [41]	46.3	46.7	49.3	49.9
	MLFN [59]	52.8	47.8	54.7	49.2
	DaRe [58]	55.1	51.3	58.1	53.7
SPF-based	HA-CNN [6]	41.7	38.6	44.4	41.0
	PCB+RPP [7]	63.7	57.5	-	-
	HPDN [62]	-	-	64.3	58.2
	CDPM	71.6	66.9	75.7	70.9
MGF	HPM [8]	63.9	57.5	-	-
	MGN [5]	66.8	66.0	68.0	67.4
	CDPM*	78.6	73.3	81.1	77.2

D. Ablation Study

In the following, we conduct ablation study to justify the effectiveness of each newly introduced component in CDPM, i.e., the vertical alignment module and horizontal refinement module. Moreover, we also compare some possible variants of the vertical alignment module and design experiments to evaluate the influence of the annotation to the performance of CDPM. Following recent works [6], [7], ablation study is conducted on both the Market-1501 and DukeMTMC-ReID.

1) *Effectiveness of the Vertical Alignment Module:* We equip the baseline model with the vertical alignment module and denote this model as Baseline+V in Table IV. As shown in Table IV, equipping the vertical alignment module consistently promotes ReID performance. In particular, Baseline+V outperforms the baseline model by 1.1% and 1.4% in Rank-1 accuracy on Market-1501 and DukeMTMC-ReID, respectively. Moreover, exemplars of body-part detection results by the vertical alignment module are illustrated in Fig. 8. It is clear that the vertical alignment module can detect body parts rather robustly against severe mis-alignment, occlusion, and pose variations. The above experiments justify the effectiveness of the vertical alignment module.

2) *Effectiveness of the Horizontal Refinement Module:* We equip the baseline model with the horizontal refinement module only, which is denoted as Baseline+H in Table IV. It is



Fig. 8. The vertical alignment module can detect body part robustly under a vast majority of circumstances, including moderate (a, b) or even severe (c, d) part mis-alignment, dramatic pose variations (e, f), and occlusion (g). The vertical alignment module may fail when there is complex occlusion or a part missing problem (h). Best viewed in color.

worth recalling that Baseline+H applies one SCA [6] module to each part-level feature learning branch. As shown in Table IV, the horizontal refinement module consistently improves the performance of baseline. For example, it improves the Rank-1 accuracy on Market-1501 from 93.5% to 94.7%, which means a 18.5% relative reduction in the error rate.

Similar to [6], we also try to apply only one SCA module to the whole feature maps output by the backbone model, which is denoted as Baseline+H(G) in Table IV. Experimental results indicate that Baseline+H consistently outperforms Baseline+H(G). This result justifies our motivation that it is much easier to reduce the interference of background in a *divide-and-conquer* manner.

Finally, we simultaneously equip the baseline model with both modules. The results are in the row CDPM in Table IV. It is clear that the combination of two modules can further promote the performance considerably. Compared with the baseline model, CDPM boosts the Rank-1 accuracy by 1.8% and 2.4%, and mAP by 4.3% and 3.1%, on Market-1501 and DukeMTMC-ReID, respectively. The above comparisons mean that the vertical alignment module and horizontal refinement module are complementary; therefore, the proposed *divide-and-conquer* solution is effective.

3) *Structure of the Vertical Alignment Module:* We compare the performance of the vertical alignment module with two possible variants. Similar to Faster-RCNN [50], the first variant (denoted as Variant 1 in Table V) shares parameters of the 1×1 convolutional layer of the coarse classification task and K refined regression tasks. The second variant (denoted as Variant 2 in Table V) shares parameters of the 1×1 convolutional layer between each part-level feature learning branch and the corresponding refined regression task in the vertical alignment module. As shown in Table V, both variants are inferior to CDPM. For example, the Rank-1 accuracies of the

TABLE IV

EVALUATION OF THE EFFECTIVENESS OF EACH COMPONENT IN CDPM. V DENOTES THE VERTICAL ALIGNMENT MODULE AND H DENOTES THE HORIZONTAL REFINEMENT MODULE¹.

Dataset	Market-1501		DukeMTMC-ReID	
Metric	Rank-1	mAP	Rank-1	mAP
Baseline	93.5	81.9	86.0	74.5
Baseline+V	94.6	84.4	87.4	76.3
Baseline+H	94.7	84.8	87.7	76.7
Baseline+H(G)	94.0	83.6	86.5	75.4
CDPM	95.3	86.2	88.4	77.6

two variants on Market-1501 are lower than CDPM by 0.8% and 3.0%, respectively. The above results provide two insights. First, in contrast with object detection [50], body part detection is a fine-grained task; therefore more independent parameters are required for each specific part detection task. Second, part-level feature learning for recognition and body part detection are heterogenous tasks. The former learns the unique character of one identity. The latter is based on the general character of one specific body part among different identities. Therefore, the two tasks should not share parameters.

TABLE V

PERFORMANCE COMPARISONS OF VARIANTS FOR THE VERTICAL ALIGNMENT MODULE.

Dataset	Market-1501		DukeMTMC-ReID	
Metric	Rank-1	mAP	Rank-1	mAP
Baseline	93.5	81.9	86.0	74.5
Variant 1	94.5	85.7	87.5	76.2
Variant 2	92.3	81.0	85.2	73.3
CDPM	95.3	86.2	88.4	77.6

4) *Amount of Annotations*: In the above experiments, we assume that annotation is provided for the entire training set. In the following, we show that CDPM still achieves competitive performance using partial but adequate annotations. As shown in Fig. 9, four annotation proportions, i.e., 25%, 50%, 75%, and 100% are evaluated. During training, only the annotated images are employed to optimize the vertical alignment module of CDPM. Experimental results show that when the annotation proportion is reduced to 75%, the mAP value by CDPM drops only by 0.1% and 0.2% on Market-1501 and DukeMTMC-ReID databases, respectively. The Rank-1 accuracy drops only by 0.2% and 0.1% on the two datasets, respectively. However, when the amount of annotation is reduced to 25%, there is an obvious drop in performance. This is because the number of images with annotation is too small, i.e., 12 images on average for each batch in our setting, which degrades the optimization quality of the vertical alignment module. The above results show that CDPM can perform well even with partial but adequate annotations, making it easy to use in real-world applications.

V. CONCLUSION

In this work we study the part mis-alignment problem in person ReID and propose a novel framework named CDPM

¹For fair comparison, all models in Table IV are trained with the same number of epochs.

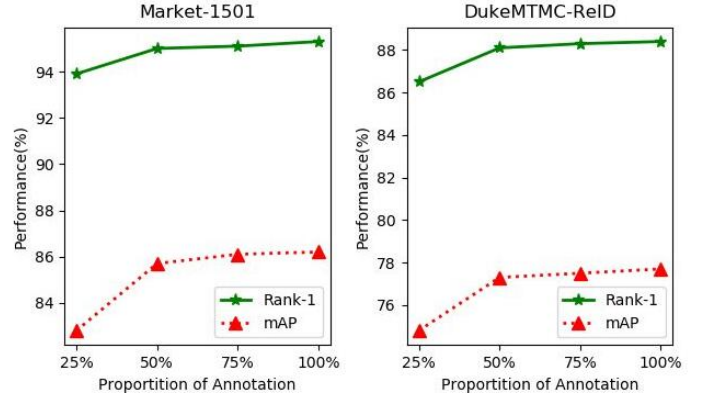


Fig. 9. The Rank-1 accuracy and mAP of CDPM trained with different annotation proportions.

that integrates part-level feature learning and part alignment in a single succinct model. In contrast with existing works, we decouple the complicated part mis-alignment problem into two orthogonal and sequential steps. The first step detects body parts in the vertical direction and the second step separately refines the boundary of each body part in the horizontal direction. Thanks to the *divide-and-conquer* strategy, each of the two steps becomes significantly simpler. We conduct extensive experiments on three large-scale ReID benchmarks, where the effectiveness of the proposed model is justified and state-of-the-art performance is achieved. We also provide detailed ablation study to show the effectiveness of each component in the proposed model.

REFERENCES

- [1] E. Ristani and C. Tomasi, "Features for multi-target multi-camera tracking and re-identification," in *Proc. IEEE Conf. Comput. Vis. Pattern Recognit.*, 2018, pp. 6036–6046.
- [2] L. Zheng, H. Zhang, S. Sun, M. Chandraker, Y. Yang, and Q. Tian, "Person re-identification in the wild," in *Proc. IEEE Conf. Comput. Vis. Pattern Recognit.*, 2017, pp. 1367–1376.
- [3] L. Zheng, Y. Yang, and A. G. Hauptmann, "Person re-identification: Past, present and future," *arXiv preprint arXiv:1610.02984*, 2016.
- [4] H. Yao, S. Zhang, Y. Zhang, J. Li, and Q. Tian, "Deep representation learning with part loss for person re-identification," *IEEE Trans. Image Process.*, 2019.
- [5] G. Wang, Y. Yuan, X. Chen, J. Li, and X. Zhou, "Learning discriminative features with multiple granularities for person re-identification," in *Proc. ACM Int. Conf. Multimedia*, 2018, pp. 274–282.
- [6] W. Li, X. Zhu, and S. Gong, "Harmonious attention network for person re-identification," in *Proc. IEEE Conf. Comput. Vis. Pattern Recognit.*, 2018, pp. 2285–2294.
- [7] Y. Sun, L. Zheng, Y. Yang, Q. Tian, and S. Wang, "Beyond part models: Person retrieval with refined part pooling (and a strong convolutional baseline)," in *Proc. Eur. Conf. Comput. Vis.*, 2018, pp. 480–496.
- [8] Y. Fu, Y. Wei, Y. Zhou, H. Shi, G. Huang, X. Wang, Z. Yao, and T. Huang, "Horizontal pyramid matching for person re-identification," in *Proc. AAAI*, 2019.
- [9] F. Zhu, X. Kong, L. Zheng, H. Fu, and Q. Tian, "Part-based deep hashing for large-scale person re-identification," *IEEE Trans. Image Process.*, vol. 26, no. 10, pp. 4806–4817, 2017.
- [10] X. Zhang, H. Luo, X. Fan, W. Xiang, Y. Sun, Q. Xiao, W. Jiang, C. Zhang, and J. Sun, "Alignedreid: Surpassing human-level performance in person re-identification," *arXiv preprint arXiv:1711.08184*, 2017.
- [11] Z. Zheng, L. Zheng, and Y. Yang, "Pedestrian alignment network for large-scale person re-identification," *IEEE Trans. Syst., Man, Cybern., Syst.*, 2018.

- [12] H. Zhao, M. Tian, S. Sun, J. Shao, J. Yan, S. Yi, X. Wang, and X. Tang, "Spindle net: Person re-identification with human body region guided feature decomposition and fusion," in *Proc. IEEE Conf. Comput. Vis. Pattern Recognit.*, 2017, pp. 1077–1085.
- [13] C. Su, J. Li, S. Zhang, J. Xing, W. Gao, and Q. Tian, "Pose-driven deep convolutional model for person re-identification," in *Proc. IEEE Int. Conf. Comput. Vis.*, 2017, pp. 3960–3969.
- [14] D. Li, X. Chen, Z. Zhang, and K. Huang, "Learning deep context-aware features over body and latent parts for person re-identification," in *Proc. IEEE Conf. Comput. Vis. Pattern Recognit.*, 2017, pp. 384–393.
- [15] X. Lan, H. Wang, S. Gong, and X. Zhu, "Deep reinforcement learning attention selection for person re-identification," in *Proc. Bri. Mach. Vis. Conf.*, 2017, pp. 4–7.
- [16] L. Zhao, X. Li, Y. Zhuang, and J. Wang, "Deeply-learned part-aligned representations for person re-identification," in *Proc. IEEE Int. Conf. Comput. Vis.*, 2017, pp. 3219–3228.
- [17] X. Liu, H. Zhao, M. Tian, L. Sheng, J. Shao, S. Yi, J. Yan, and X. Wang, "Hydraplus-net: Attentive deep features for pedestrian analysis," in *Proc. IEEE Int. Conf. Comput. Vis.*, 2017, pp. 350–359.
- [18] S. Zhang, J. Yang, and B. Schiele, "Occluded pedestrian detection through guided attention in cnns," in *Proc. IEEE Conf. Comput. Vis. Pattern Recognit.*, 2018, pp. 6995–7003.
- [19] L. Zheng, L. Shen, L. Tian, S. Wang, J. Wang, and Q. Tian, "Scalable person re-identification: A benchmark," in *Proc. IEEE Int. Conf. Comput. Vis.*, 2015, pp. 1116–1124.
- [20] Z. Zheng, L. Zheng, and Y. Yang, "Unlabeled samples generated by gan improve the person re-identification baseline in vitro," in *Proc. IEEE Int. Conf. Comput. Vis.*, 2017, pp. 3754–3762.
- [21] W. Li, R. Zhao, T. Xiao, and X. Wang, "Deepreid: Deep filter pairing neural network for person re-identification," in *Proc. IEEE Conf. Comput. Vis. Pattern Recognit.*, 2014, pp. 152–159.
- [22] R. R. Viorio, G. Wang, J. Lu, and T. Liu, "Learning invariant color features for person re-identification," *IEEE Trans. Image Process.*, vol. 25, no. 7, pp. 3395–3410, 2016.
- [23] R. Zhao, W. Ouyang, and X. Wang, "Unsupervised salience learning for person re-identification," in *Proc. IEEE Conf. Comput. Vis. Pattern Recognit.*, 2013, pp. 3586–3593.
- [24] J. Chen, Z. Zhang, and Y. Wang, "Relevance metric learning for person re-identification by exploiting listwise similarities," *IEEE Trans. on Image Process.*, vol. 24, no. 12, pp. 4741–4755, 2015.
- [25] J. Garcia, N. Martinel, A. Gardel, I. Bravo, G. L. Foresti, and C. Micheloni, "Discriminant context information analysis for post-ranking person re-identification," *IEEE Trans. Image Process.*, vol. 26, no. 4, pp. 1650–1665, 2017.
- [26] J. Chen, Z. Zhang, and Y. Wang, "Relevance metric learning for person re-identification by exploiting listwise similarities," *IEEE Trans. Image Process.*, vol. 24, no. 12, pp. 4741–4755, 2015.
- [27] B. Nguyen and B. De Baets, "Kernel distance metric learning using pairwise constraints for person re-identification," *IEEE Trans. Image Process.*, vol. 28, no. 2, pp. 589–600, 2019.
- [28] X. Yang, M. Wang, and D. Tao, "Person re-identification with metric learning using privileged information," *IEEE Trans. Image Process.*, vol. 27, no. 2, pp. 791–805, 2018.
- [29] Z. Feng, J. Lai, and X. Xie, "Learning view-specific deep networks for person re-identification," *IEEE Trans. Image Process.*, vol. 27, no. 7, pp. 3472–3483, 2018.
- [30] J. Dai, P. Zhang, D. Wang, H. Lu, and H. Wang, "Video person re-identification by temporal residual learning," *IEEE Trans. Image Process.*, vol. 28, no. 3, pp. 1366–1377, 2019.
- [31] H. Liu, J. Feng, M. Qi, J. Jiang, and S. Yan, "End-to-end comparative attention networks for person re-identification," *IEEE Trans. Image Process.*, vol. 26, no. 7, pp. 3492–3506, 2017.
- [32] A. Wu, W.-S. Zheng, and J.-H. Lai, "Robust depth-based person re-identification," *IEEE Trans. Image Process.*, vol. 26, no. 6, pp. 2588–2603, 2017.
- [33] S.-Z. Chen, C.-C. Guo, and J.-H. Lai, "Deep ranking for person re-identification via joint representation learning," *IEEE Trans. Image Process.*, vol. 25, no. 5, pp. 2353–2367, 2016.
- [34] R. R. Viorio, B. Shuai, J. Lu, D. Xu, and G. Wang, "A siamese long short-term memory architecture for human re-identification," in *Proc. Eur. Conf. Comput. Vis.*, 2016, pp. 135–153.
- [35] A. Hermans, L. Beyer, and B. Leibe, "In defense of the triplet loss for person re-identification," *arXiv preprint arXiv:1703.07737*, 2017.
- [36] W. Chen, X. Chen, J. Zhang, and K. Huang, "Beyond triplet loss: a deep quadruplet network for person re-identification," in *Proc. IEEE Conf. Comput. Vis. Pattern Recognit.*, 2017, pp. 403–412.
- [37] C. Wang, Q. Zhang, C. Huang, W. Liu, and X. Wang, "Manacs: A multi-task attentional network with curriculum sampling for person re-identification," in *Proc. Eur. Conf. Comput. Vis.*, 2018, pp. 365–381.
- [38] W. Chen, X. Chen, J. Zhang, and K. Huang, "A multi-task deep network for person re-identification," in *Proc. AAAI*, 2017.
- [39] E. Ahmed, M. Jones, and T. K. Marks, "An improved deep learning architecture for person re-identification," in *Proc. IEEE Conf. Comput. Vis. Pattern Recognit.*, 2015, pp. 3908–3916.
- [40] D. Cheng, Y. Gong, S. Zhou, J. Wang, and N. Zheng, "Person re-identification by multi-channel parts-based cnn with improved triplet loss function," in *Proc. IEEE Conf. Comput. Vis. Pattern Recognit.*, pp. 1335–1344.
- [41] C. Song, Y. Huang, W. Ouyang, and L. Wang, "Mask-guided contrastive attention model for person re-identification," in *Proc. IEEE Conf. Comput. Vis. Pattern Recognit.*, 2018, pp. 1179–1188.
- [42] M. Tian, S. Yi, H. Li, S. Li, X. Zhang, J. Shi, J. Yan, and X. Wang, "Eliminating background-bias for robust person re-identification," in *Proc. IEEE Conf. Comput. Vis. Pattern Recognit.*, 2018, pp. 5794–5803.
- [43] M. M. Kalayeh, E. Basaran, M. Gökmen, M. E. Kamasak, and M. Shah, "Human semantic parsing for person re-identification," in *Proc. IEEE Conf. Comput. Vis. Pattern Recognit.*, 2018, pp. 1062–1071.
- [44] J. Xu, R. Zhao, F. Zhu, H. Wang, and W. Ouyang, "Attention-aware compositional network for person re-identification," in *Proc. IEEE Conf. Comput. Vis. Pattern Recognit.*, 2018, pp. 2119–2128.
- [45] P. Felzenszwalb, D. McAllester, and D. Ramanan, "A discriminatively trained, multiscale, deformable part model," in *Proc. IEEE Conf. Comput. Vis. Pattern Recognit.*, 2008.
- [46] W. Ouyang, X. Wang, X. Zeng, S. Qiu, P. Luo, Y. Tian, H. Li, S. Yang, Z. Wang, C.-C. Loy *et al.*, "Deepid-net: Deformable deep convolutional neural networks for object detection," in *Proc. IEEE Conf. Comput. Vis. Pattern Recognit.*, 2015, pp. 2403–2412.
- [47] P.-A. Savalle, S. Tsogkas, G. Papandreou, and I. Kokkinos, "Deformable part models with cnn features," in *Proc. Eur. Conf. Comput. Vis. Workshops*, 2014.
- [48] R. Girshick, F. Iandola, T. Darrell, and J. Malik, "Deformable part models are convolutional neural networks," in *Proc. IEEE Conf. Comput. Vis. Pattern Recognit.*, 2015, pp. 437–446.
- [49] R. Girshick, "Fast r-cnn," in *Proc. IEEE Int. Conf. Comput. Vis.*, 2015, pp. 1440–1448.
- [50] S. Ren, K. He, R. Girshick, and J. Sun, "Faster r-cnn: Towards real-time object detection with region proposal networks," *IEEE Trans. Pattern Anal. Mach. Intell.*, vol. 39, no. 6, p. 1137, 2017.
- [51] V. Vapnik and R. Izmailov, "Learning using privileged information: similarity control and knowledge transfer," *J. Mach. Learn. Res.*, vol. 16, no. 2023–2049, p. 2, 2015.
- [52] K. He, X. Zhang, S. Ren, and J. Sun, "Deep residual learning for image recognition," in *Proc. IEEE Conf. Comput. Vis. Pattern Recognit.*, 2016, pp. 770–778.
- [53] J. Hu, L. Shen, and G. Sun, "Squeeze-and-excitation networks," in *Proc. IEEE Conf. Comput. Vis. Pattern Recognit.*, 2018, pp. 7132–7141.
- [54] Z. Zhong, L. Zheng, D. Cao, and S. Li, "Re-ranking person re-identification with k-reciprocal encoding," in *Proc. IEEE Conf. Comput. Vis. Pattern Recognit.*, 2017, pp. 1318–1327.
- [55] Z. Zhong, L. Zheng, G. Kang, S. Li, and Y. Yang, "Random erasing data augmentation," *arXiv preprint arXiv:1708.04896*, 2017.
- [56] I. Sutskever, J. Martens, G. E. Dahl, and G. E. Hinton, "On the importance of initialization and momentum in deep learning," *Proc. Int. Conf. Mach. Learn.*, vol. 28, no. 1139–1147, p. 5.
- [57] Y. Sun, L. Zheng, W. Deng, and S. Wang, "Svdnet for pedestrian retrieval," in *Proc. IEEE Int. Conf. Comput. Vis.*, 2017, pp. 3800–3808.
- [58] Y. Wang, L. Wang, Y. You, X. Zou, V. Chen, S. Li, G. Huang, B. Hariharan, and K. Q. Weinberger, "Resource aware person re-identification across multiple resolutions," in *Proc. IEEE Conf. Comput. Vis. Pattern Recognit.*, 2018, pp. 8042–8051.
- [59] X. Chang, T. M. Hospedales, and T. Xiang, "Multi-level factorisation net for person re-identification," in *Proc. IEEE Conf. Comput. Vis. Pattern Recognit.*, 2018, pp. 2109–2118.
- [60] Y. Suh, J. Wang, S. Tang, T. Mei, and K. M. Lee, "Part-aligned bilinear representations for person re-identification," in *Proc. Eur. Conf. Comput. Vis.*, 2018, pp. 402–419.
- [61] Y. Chen, X. Zhu, and S. Gong, "Person re-identification by deep learning multi-scale representations," in *Proc. IEEE Int. Conf. Comput. Vis.*, 2017, pp. 2590–2600.
- [62] Z. Zhang and M. Huang, "Person re-identification based on heterogeneous part-based deep network in camera networks," *IEEE Trans. Emerg. Topics in Comput. Intell.*, 2018.